Characterization of grain boundary character distribution in cemented carbides *via* a stereological method

Xiaokun Yuan*, Yuan Ji

Faculty of Materials and Manufacturing, Beijing University of Technology, Beijing 100124, China

Abstract

This paper reports the interdisciplinary approach of simultaneous use of a stereological method, namely the five parameter analysis (FPA) method and the grain boundary character distribution (GBCD) in cemented carbides. There are six major aspects: i) the background and motivations of the interdisciplinary approach, ii) the principle of the FPA method, iii) orientation texture of boundary planes with specific misorientations via $\lambda(\Delta g, n)$ mode in cemented carbide, iv) orientation texture of habit planes regardless of misorientations via $\lambda(n)$ mode in cemented carbide, v) application of the FPA method to serial cemented carbide samples and vi) boundary sort methods before using the FPA method. The work aims at presenting beneficial reference for studying structural and distribution features of special coincidence site lattice (CSL) boundaries in a statistical manner, and in turn increasing the knowledge about the structure-property relationship in cemented carbides.

Keywords: grain boundary character distribution, cemented carbide, five parameter analysis

I. Introduction

Cemented carbide is a kind of cermet material that is widely used in cutting, machining, mining and drilling fields due to its excellent properties of hardness, wear resistance and fracture strength. The major constituents of the cemented carbides are the hard and brittle carbide phase (for example, tungsten carbide, for increasing wear resistance) dispersed in the soft and ductile binder phases (for example, cobalt, for increasing toughness). Spontaneously, two major boundary types in cemented carbides should be observed: the one is carbide/carbide grain boundary (the boundary between carbide phases) and the other is carbide/binder phase boundary (the boundary between carbide phase and binder phase).

For carbide/carbide grain boundary, coincidence site lattice (CSL) model is generally used to describe the lattice arrangement at the carbide/carbide boundary locations (with a Σ value representing the reciprocal density of coinciding lattice sites). For tungsten carbide, disregarding equivalents, 50 kinds of CSL boundaries can occur theoretically (Table 1) [1–3]. Compared with the random distribution [4], the $\Sigma 2$ boundary, which has a 90°/[10$\bar{1}$0] misorientation, is found to be the most

frequently occurring boundary type. Since the c/a ratio of tungsten carbide (0.976) is not exactly equal to 1, strictly speaking, $\Sigma 2$ boundary is a kind of "approximate" CSL boundary. Studies about $\Sigma 2$ boundary mainly concern the lattice features of $\Sigma 2$ boundary [5–8], lattice defects accompanied by $\Sigma 2$ boundary [9], formation and development of $\Sigma 2$ boundary [10,11] as well as the response of $\Sigma 2$ boundary to plastic deformation [12].

For the carbide/binder phase boundary, studies mainly concern the interaction between carbide phase and binder phase, which includes coating [13,14], penetration [15] and wetting [16] of binder phase to carbide phase. Meanwhile, different from the ordinary bulk phases, specific interfacial phases (named as "complexion") are in existence especially at carbide/binder phase boundary locations and exhibit equilibrium thermodynamic states. It has been addressed that the formation energy of carbide phase can be affected by doping of certain additives at phase boundary locations [17–21].

At the locations of either carbide/carbide grain boundaries or carbide/binder phase boundaries, anisotropies, that is, property difference by referring to the orientation or Miller index of crystallographic planes, are intact [22]. Among these anisotropies, energy anisotropy [23,24] would determine the boundary

* Corresponding authors: tel: +86 10 67396563,
  e-mail: *yuanxiaokun@bjut.edu.cn*

Table 1. CSL boundaries in cemented carbides

Σ value	Misorientation angle	Σ value	Misorientation angle
Σ2	90°	Σ22a	32.764°
Σ4	60°	Σ22b	45.207°
Σ5	53.130°	Σ22c	83.745°
Σ7a-1	21.787°	Σ23a	50.918°
Σ7a-2	81.787°	Σ23b	66.694°
Σ7a-3	46.567°	Σ25a	51.684°
Σ7b	81.790°	Σ25b	73.740°
Σ10a	36.870°	Σ25c	91.146°
Σ10b	69.513°	Σ28a	21.790°
Σ11	76.863°	Σ28b	38.210°
Σ13a	27.796°	Σ31	42.100°
Σ13a-near	30°	Σ37	69.430°
Σ13b	32.204°	Σ43	75.180°
Σ13c	67.380°	Σ49	16.430°
Σ14a	41.410°	Σ52a	27.800°
Σ14b	92.047°	Σ52b	87.800°
Σ16a	57.910°	Σ61	52.660°
Σ16b	82.819°	Σ67	24.420°
Σ17a	28.072°	Σ73	71.640°
Σ17b	63.821°	Σ76a	73.170°
Σ19a	13.174°	Σ76b	13.170°
Σ19b	46.826°	Σ79	26.010°
Σ19c	74.742°	Σ91a	49.580°
Σ20a	28.955°	Σ91b	66.010°
Σ20b	76.997°	Σ97	89.410°

behaviour at both fabrication and employment stage, and shape anisotropy (for example, the equiaxed-like or plate-like morphology of carbide crystals) [25–27] can be regarded as the consequence of population difference of different crystallographic planes. On a statistical level, performance control of cemented carbides via optimization of anisotropies at boundary locations is the so-called "grain boundary engineering" [28,29], which mainly considers CSL boundaries with Σ values lower than 30.

From the perspective of methodology, electron backscatter diffraction (EBSD) is the technique that transfers the detected Kikuchi patterns to the crystal orientation information *via* the Hough conversion. The orientation of carbide crystals and in-turn, orientation difference across the carbide/carbide grain boundaries (i.e. misorientation) can be measured *via* EBSD [30,31]. Besides, more structural information in cemented carbides, e.g. carbide grain growth during sintering [32], carbide size [33,34], contiguity of carbide phases [35], crack propagation along boundaries [36], hardness of cemented carbides [37], response to plastic deformation [38] and wear behaviour [39], can also be analysed from planar EBSD datasets.

It should be noted that EBSD technique for characterizing cemented carbides has underwent rapid development in the past decade. As to measurement hardware, EBSD compatible with focused ion beam (FIB) [40,41] or broad ion beam (BIB) [42] provides serial EBSD datasets and makes 3D structural characterization (3D EBSD) possible; *in situ* EBSD technique [43,44] makes real-time and dynamic observing practicable; and EBSD incorporated with scanning transmission electron microscopy (STEM) [45] enhances the resolution of EBSD datasets. As to computational approaches, interface structures [46–48], surface energy [49] and sliding resistance [50] for specific boundaries can be modelled and investigated, and new computational techniques [51–53] have enabled mutual corroboration with virtual EBSD measurements.

To evaluate techniques for characterizing crystals in cemented carbides, several factors should be taken into account: i) the speed for data collecting, or how many crystals can be recorded per time, ii) the floor limit about the grain size, which would determine the precision of the collected data and iii) the info capacity of the data, that is, what kind of structural info can be obtained from the data. For EBSD technique, if the data is based on a certain number of crystals, orientation texture of crystals can be characterized. Furthermore, since there also exist boundary networks between crystals, correspondingly, there should exist orientation texture of boundary planes. Therefore, this work mainly concerns: i) boundary attributes including lattice structure and orientation textures in cemented carbides and ii) characterizing approaches and their applications for boundaries in

cemented carbides. For readers' convenience, experimental results in this work come from randomly selected cemented carbide samples without definite relationship, while these samples have no overlap with the previous reports.

II. The principle of the FPA method

Compared to abundant studies about orientation texture of crystals, studies about orientation texture of boundary planes in polycrystalline remain limited. Since year 2000, the five parameter analysis (FPA) method, developed by Carnegie Mellon University, has received broader applications and has validated its veracity for studying orientation texture of boundary planes in various subjects. The so-called "five parameter(s)" means that in order to completely characterize the orientation of a boundary plane, five macroscopic degrees of freedom (for describing rotation axis, rotation angle and boundary plane normal) should be considered [54]. In the FPA method, five angular parameters are commonly used: three angular parameters (for example, three Eulerian angles) are used to describe the misorientation across the boundary plane (in FPA, they are marked as Δg), and the remaining two angular parameters are used to describe the direction of boundary plane normal in the crystallographic frame (in FPA, they are remarked as n) [55,56]. As a statistical approach, the FPA method does not characterize detailed crystallographic attributes of a specific boundary, but presents statistical information correlated to misorientations across boundary planes.

Table 2. Requirement of line segments of the FPA method

Lattice symmetry	Line segments number requirement	
	$\lambda(\Delta g, n)$ mode	$\lambda(n)$ mode
cubic	0.5×10^4	0.2×10^4
hexagonal	20×10^4	0.5×10^4
tetragonal	45×10^4	1×10^4
trigonal	180×10^4	1×10^4

There are two major modes for the FPA method: i) when all the five angular parameters are taken into account then the $\lambda(\Delta g, n)$ mode is suitable for studying the orientation texture for boundary planes with a specific misorientation and ii) when the misorientation is averaged (or, ignored), the $\lambda(n)$ mode is suitable for studying the orientation texture for habit planes. Requirement of line segments number differs according to the lattice symmetry and the working mode (Table 2). For $\lambda(\Delta g, n)$ mode, a program named GBToolBox facilitates the calibration of occurring locations of the geometrically characteristic boundaries, and the program would define the boundary structure as twist, tilt, 180°-twist (symmetric) or 180°-tilt (improperly quasi-symmetric) [57,58].

The use of the FPA method in cemented carbides has been elaborated in Ref. [59–61]. For readers' conve-

nience, taking $\lambda(\Delta g, n)$ mode of $\Sigma 2$ boundary as an example, the basic steps for the FPA method can be summarized as:

(1) Before the FPA method: i) observe enough crystal pairs that have indistinguishable misorientations, with crystals oriented differently with respect to the observation plane, ii) the collected planar EBSD data undergoes a clean-up procedure to ensure the reliable orientation assignments for small carbide crystals and iii) enough line segments are extracted from the orientation map according to the misorientation across the boundary and are associated with the crystal orientations.

(2) During the FPA method: i) each line segment generates a set of possible boundary planes that contain this line segment, ii) classify the probability, that is, the probability that each boundary plane set contains the true boundary plane is one, while the probability that each boundary plane set include any arbitrary plane is less than one, iii) give multiple observations of the same type of bicrystal, that is, concentrate on the bicrystals with 90°/[10$\bar{1}$0] misorientation relationship in this example, and as the consequence, true $\Sigma 2$ boundary planes would make up a relatively larger fraction in the accumulated data than that of the random boundary planes, and can in-turn be identified as peaks in the distribution and iv) remove the inhomogeneous background caused by the incorrect planes and therefore, the ratios of the observed line lengths can specify the relative areas of $\Sigma 2$ boundary type, that is, $\lambda(\Delta g, n)$ of $\Sigma 2$ boundary.

(3) After the FPA method, i.e. visualization of the FPA result: $\lambda(\Delta g, n)$ means that the statistically analysed orientation texture of boundary planes and the outcomes are plotted as a pole plot according to the following steps: i) spherical projection of the boundary plane normals in the crystallographic frame (Fig. 1a), ii) the corresponding stereographic projection (Fig. 1b), iii) in the pole plot, orientation preference of boundary plane normals can be classified and the corresponding texture intensities can be calibrated in units of multiples of a random distribution (MRD, Fig. 1c) and iv) analyse the boundary structure by comparing it with the GBToolBox result of the corresponding misorientation relationship (Fig. 1d).

III. Application of $\lambda(\Delta g, n)$ mode to cemented carbide

As stated before, the $\lambda(\Delta g, n)$ mode takes both Δg and n into account and the corresponding result illustrates the orientation texture for boundary planes with the investigated misorientation.

To read a single $\lambda(\Delta g, n)$ pole plot, three elements should be highly evaluated:

(1) The peak position, which would illustrate the boundary structure, in other words, the most frequently occurred boundary plane normal would show the structural feature of that misorientation (according to whether it is exactly located at or slightly deviates from the ideal position): taking Fig. 1c as an example
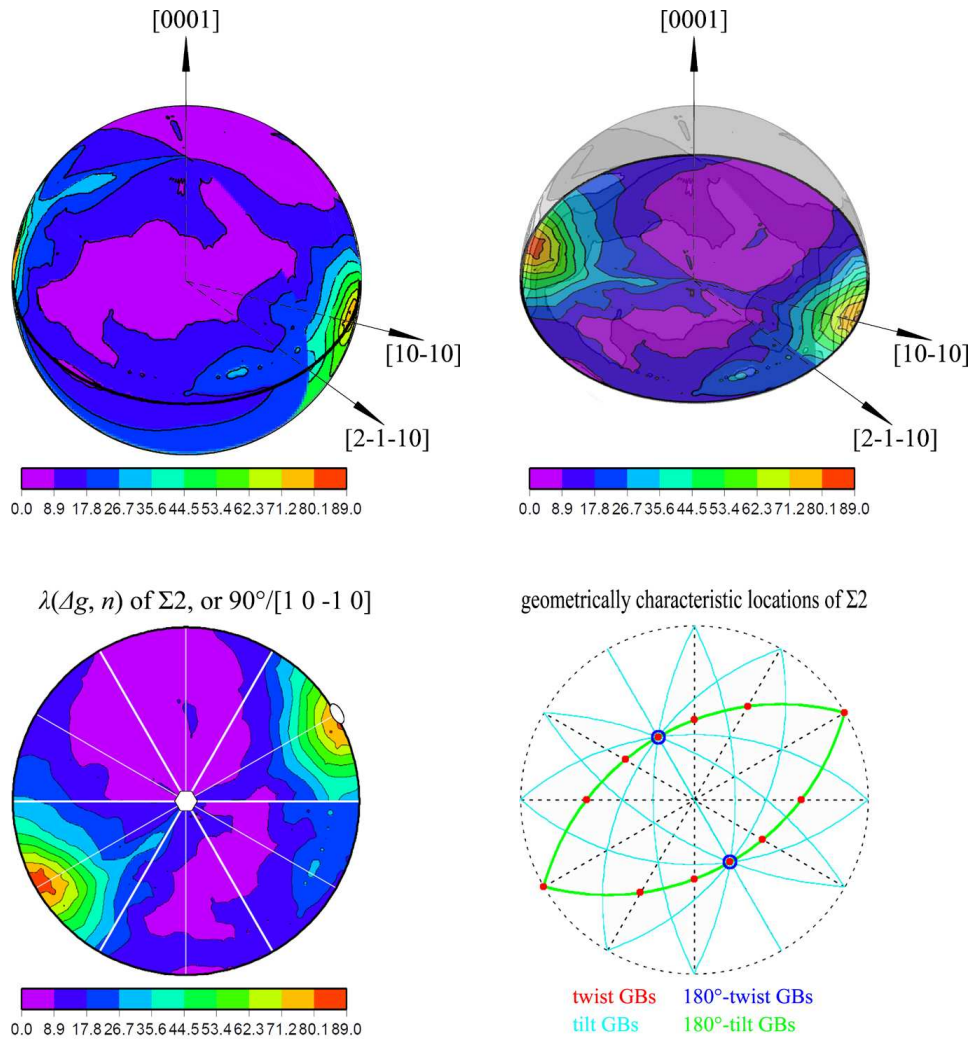
Figure 1. Visualization of the FPA result: a) spherical projection of the boundary plane normals in the crystallographic frame; b) the corresponding stereographic projection; c) orientation texture of Σ2 boundary planes, with locations corresponding to the (0001) and (10$\bar{1}$0) orientations indicated by hexagon and oval, respectively, and with units of the contours marked by MRD and d) the calculated locations of the geometrically characteristic boundaries of the Σ2 boundary *via* GBToolBox, with the *c/a* ratio of tungsten carbide set as $\sqrt{20/21}$, and with red for twist, cyan for tilt, blue for 180°-twist, green for 180°-tilt boundary locations
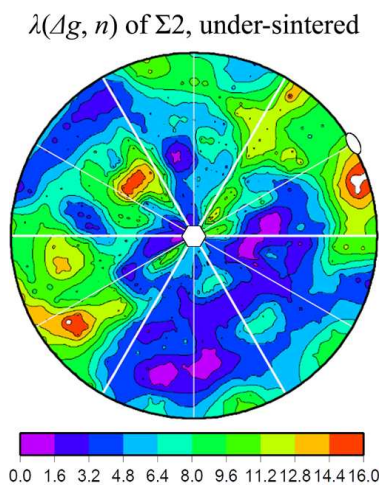

Figure 2. An observed coexistence of near-twist and 180°-twist configurations of Σ2 boundary in an under-sintered sample

and by comparing with the geometrically characteristic locations shown in Fig. 1d, it can be observed that the peak of the distribution is at the position of the corresponding [10$\bar{1}$0] misorientation axis; in turn, it can be inferred that the Σ2 boundary plane is perpendicular to the common rotation axis of the crystal pair, and therefore, the boundary has a pure twist configuration. According to Fig. 1d, if the peak locates along the great circle perpendicular to the [10$\bar{1}$0] misorientation axes, the Σ2 boundary would show a tilt configuration in this case; and if the peak is at the ($\bar{1}2\bar{1}3$) position, the Σ2 boundary would show a 180°-twist symmetric structure, and such case has been verified in some under-sintered samples. Note that various Σ2 boundary structures can coexist in a sample and their corresponding peaks can be found simultaneously in a $\lambda(\Delta g, n)$ pole plot (Fig. 2 as an example). Also note that Fig. 1d is obtained after the *c/a* ratio of tungsten carbide is virtually set as $\sqrt{20/21}$. When the *c/a* ratio of tungsten carbide is hypothetically
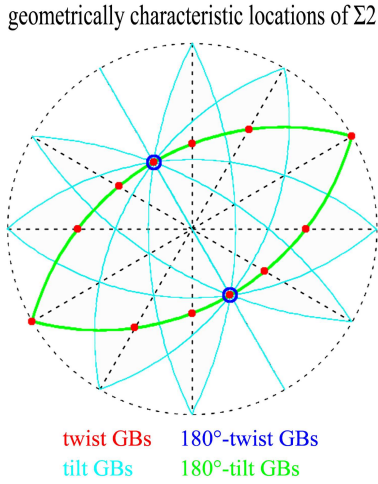
geometrically characteristic locations of Σ2

twist GBs   180°-twist GBs
tilt GBs   180°-tilt GBs

Figure 3. The calculated locations of the geometrically characteristic boundaries of the Σ2 boundary, with the *c/a* ratio of tungsten carbide set as 1, and with red for twist, cyan for tilt, blue for 180°-twist, green for 180°-tilt boundary locations

set as 1, the geometrical locations of the Σ2 boundary are kept almost the same due to the angular resolution (Fig. 3).

(2) The MRD value at the related peak position, which would show the "population" (or the occurring frequency of that misorientation) by comparing with random boundaries, and the result would illustrate the orientation texture of boundary planes. Accordingly, the

MRD value can be used to compare the occurring frequency of various boundary types in a single sample (Fig. 2 as an example) and it can also be used to compare the occurring frequency of one boundary type in a series of samples.

(3) The spreads between the peak positions, which would illustrate the existence of crystal rotation along specific zone axis and towards specific poles. Taking Σ2 twist boundary as an example: it has been well documented that Σ2 boundaries originate from the boundaries in the starting powder and their population is reduced during sintering. Moreover, the Σ2 boundaries are more prone to be evolved in the coalescence of low-energy crystallographic facets during sintering. Therefore, for the Σ2 twist boundary, the spreads between $(10\bar{1}0)$ and $(\bar{1}010)$ poles reveal the crystal rotation resulting from the coalescence of carbide grains. If carbide grains were more facilitated to rotate, there would be less spreads between $(10\bar{1}0)$ and $(\bar{1}010)$ poles, and vice versa. Figure 4 is an example: in a unit of volume, if the carbide size is fine enough (sometimes such case can be achieved *via* addition of grain growth inhibitors, GGI), the carbide crystals are facilitated to rotate to form Σ2 twist boundaries, causing poor spreads between $(10\bar{1}0)$ and $(\bar{1}010)$ poles (Fig. 4a); if the carbide size becomes larger, the crystal rotation becomes a little bit harder, causing slight spreads between $(10\bar{1}0)$ and $(\bar{1}010)$ poles (schematic Fig. 4b); if the carbide size is too large and makes the crystal rotation harder,
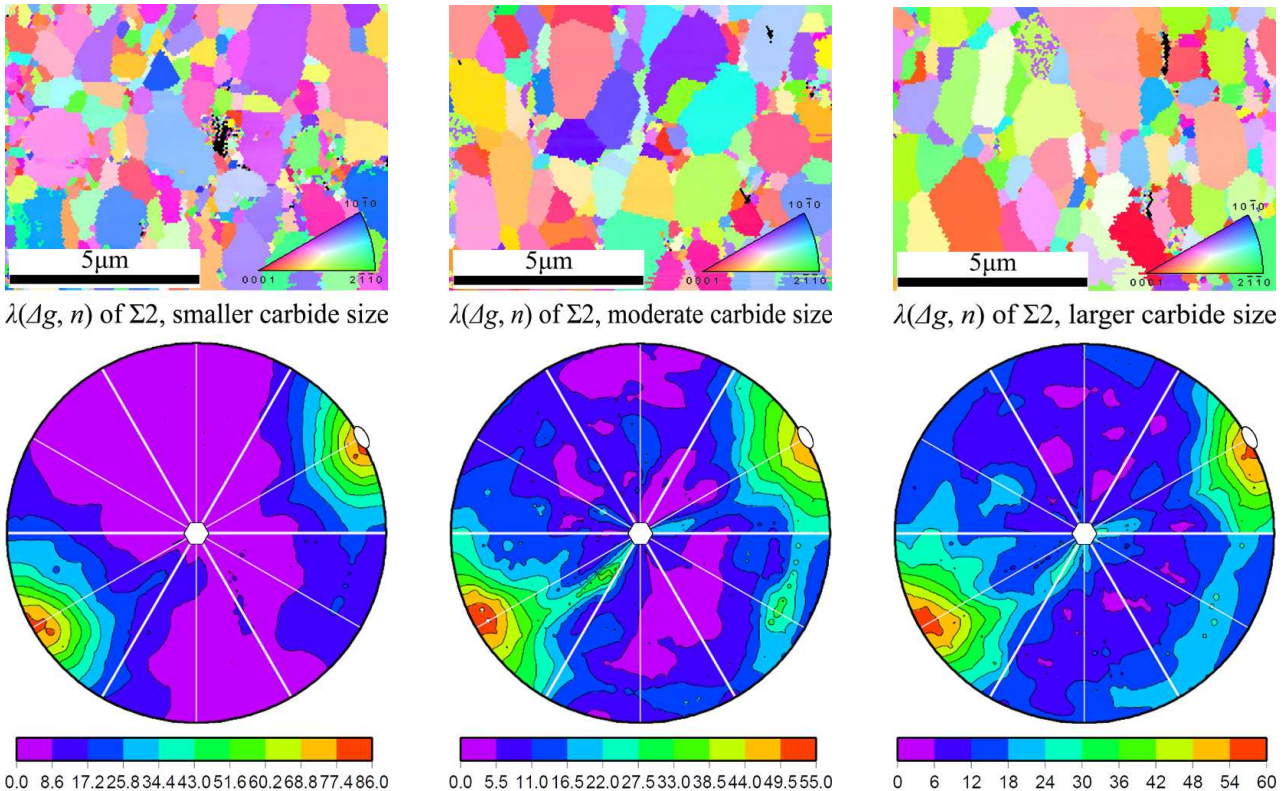

$\lambda(\Delta g, n)$ of Σ2, smaller carbide size $\lambda(\Delta g, n)$ of Σ2, moderate carbide size $\lambda(\Delta g, n)$ of Σ2, larger carbide size

0.0 8.6 17.2 25.8 34.4 43.0 51.6 60.2 68.8 77.4 86.0   0.0 5.5 11.0 16.5 22.0 27.5 33.0 38.5 44.0 49.5 55.0   0 6 12 18 24 30 36 42 48 54 60

Figure 4. Larger carbide size causes harder crystal rotation to form Σ2 twist boundary and stronger spreads between $(10\bar{1}0)$ and $(\bar{1}010)$ poles. For each case, the inverse pole figure (IPF) map with orientation legend is shown above, with the corresponding $\lambda(\Delta g, n)$ of Σ2 shown underneath: (a) the case of smaller carbide size; (b) the case of moderate carbide size; (c) the case of larger carbide size
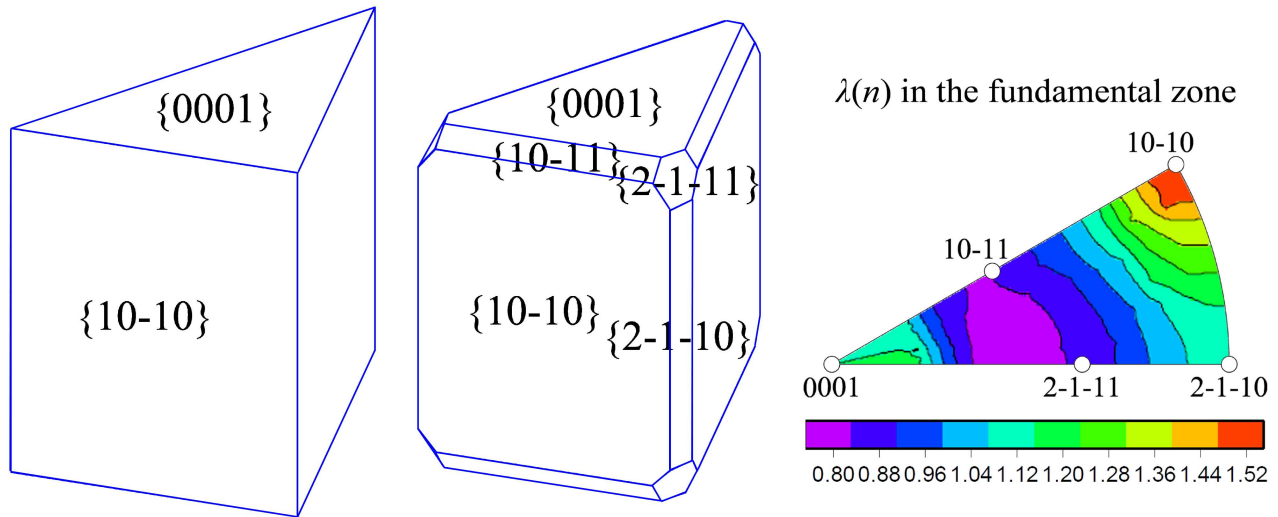
Figure 5. The idealized polygon for describing the average three-dimensional shape: a) merely consider (0001) and (10$\bar{1}$0) planes, b) comprehensively consider multiple planes and c) the relative area of each habit plane corresponds to the MRD value in the $\lambda(n)$ pole plot in the fundamental zone

the spreads between (10$\bar{1}$0) and ($\bar{1}$010) poles become stronger (Fig. 4c).

IV. Application of $\lambda(n)$ mode in cemented carbide

As stated before, the $\lambda(n)$ mode means the misorientation parameters are ignored or averaged and the corresponding result illustrates the orientation texture of habit planes.

The concept of habit planes should be addressed here. If a phase transition is involved, habit plane should refer to the crystallographic plane that has a specific mutual orientation relationship between the parent phase and the new phase. However, according to reference [62], habit plane also refers to the plane of the plate of a plate-shaped crystal, or the crystal habits [63].

Tungsten carbide belongs to the hexagonal D_{6h} symmetry, where the (0001) basal facet and the (10$\bar{1}$0) prismatic facet are the two most common habit planes. Since the $\lambda(n)$ mode of the FPA method can illustrate the occurring frequencies of these habit planes, the interface area aspect ratio, or, the ratio between the relative area of the (0001) basal plane to the relative area of the (10$\bar{1}$0) prismatic plane, can be calculated [64]. Note that since the $\lambda(n)$ mode counts more than 0.5×10^4 line segments, the interface area aspect ratio depicts the average three-dimensional shape of a batch of carbide crystals. Also note that *via* the MRD values of typical habit planes in a $\lambda(n)$ pole plot, the shape anisotropy, i.e. equiaxed-like or plate-like feature of the covered carbide crystals, can be reflected.

There exist multiple habit planes other than (0001) and (10$\bar{1}$0) planes. Accordingly, the idealized polygon for describing the average three-dimensional shape should contain not only (0001) basal and (10$\bar{1}$0) prismatic planes, but also the crystallographic planes between them [65–67]. For example: habit planes between (10$\bar{1}$0) prismatic planes, habit planes between (10$\bar{1}$0) prismatic and one (0001) basal planes, as well as the "vertex" planes between two (10$\bar{1}$0) prismatic and one (0001) basal planes. To read a single $\lambda(n)$ pole plot, the peak positions show the Miller indices of the most frequently occurred habit planes, and the corresponding MRD values show the relative population or the relative area of each habit planes (Fig. 5). It is not hard to imagine that if the habit planes have similar relative area, the studied carbide crystals would show an equiaxed-like shape; otherwise, the studied carbide crystals would show obvious shape anisotropy, for example, plate-like morphology.

V. Application of the FPA method to serial cemented carbide samples

Both the $\lambda(\Delta g, n)$ mode and the $\lambda(n)$ mode of the FPA method can be used to a series of samples, and the results can illustrate the change of grain boundary character distribution (GBCD) along with the variation of processing/application factors.

For the $\lambda(\Delta g, n)$ mode, processing factors that have been studied include different carbide size [68,69], different binder phases [70–72], different densification mechanisms [73,74], different binder fraction [75] and different sintering temperature [76]. Meanwhile, the existing literature mainly considers the alteration of GBCD under plastic deformation [77–81].

For the $\lambda(n)$ mode, the average three-dimensional shape of the studied crystals can be described *via* an idealized polygon, and the shape anisotropy of the studied crystals can be characterized. The shape anisotropy in cemented carbides has complicated origins, and strange-shaped carbide crystals in cemented carbides can often be observed. For various habit planes, their corresponding driving forces for plane developing are different, that is, the development of carbide crystals along various habit planes is anisotropic.
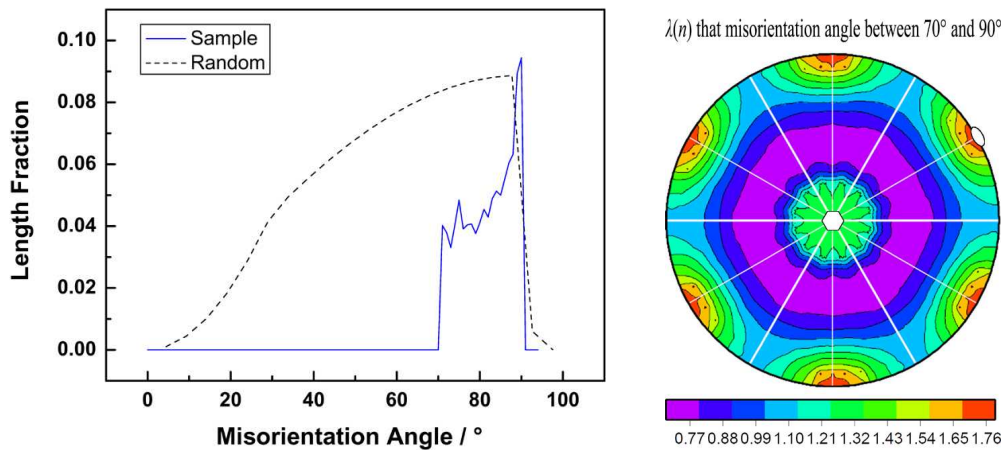
Figure 6. The carbide/carbide boundaries with misorientation angle between 70° and 90°: a) the misorientation angle statistics in blue line, with the dash line representing a randomly oriented case and b) the $\lambda(n)$ statistics of these boundaries

As stated before, *in situ* tensile EBSD observation to cemented carbide has been realized. Due to the high hardness requirement of fixture appliance, *in situ* compressed EBSD observation in cemented carbide is relatively difficult at the current stage. Nevertheless, applying the FPA method at each *in situ* observing node could expatiate the real-time evolution of GBCD along with the alteration of microstructure.

VI. Boundary sort methods before using the FPA method

In practice, boundaries with specific attributes need to be investigated alone. Accordingly, boundary subset (in which boundaries have the same attributes) needs to be sorted out from the whole boundaries. The background data of an EBSD dataset is a text file, in which each line corresponds to a line segment in the EBSD dataset, while each line contains detailed information of that line segment, and therefore, the whole boundaries can be divided into different subsets according to the information:

(1) Each line contains the crystal orientation on the two sides of the line segment and accordingly, the whole boundaries can be divided into subsets according to the misorientation across the line segment. For example: the whole boundaries can be divided into $\Sigma 2$ boundary subset (match the $90°/[10\bar{1}0]$ misorientation) and rest boundary subset (do not match the $90°/[10\bar{1}0]$ misorientation).

(2) According to the misorientation across the line segment, the whole boundaries can also be divided into subsets according to the misorientation angle range. For example: the whole boundaries can be divided into subset (have the misorientation angle between $85 \sim 95°$) and rest subset (have the misorientation angle other than $85 \sim 95°$).

(3) Each line contains phase attribute on the two sides of the line segment and accordingly, the whole boundaries can be divided into subsets corresponding to carbide/carbide grain boundaries, binder/binder grain boundaries and carbide/binder phase boundaries, respectively.

(4) Specific subsets in which each line segment has multiple attributes can be sorted out from the whole boundaries via judging whether that line segment satisfies multiple conditions. Figure 6 is an example: the carbide/carbide grain boundaries whose misorientation angle values are between 85° and 95° can be sorted out from the whole boundaries, and their corresponding $\lambda(n)$ pole plot can then be counted.

(5) Each line also contains the coordinates of the start and end points of the line segment, with the length and the trace angle of that line segment. Meanwhile, the line number means the population of the line segment. Therefore, stereological statistics can be performed to each subset, including: number fraction, length fraction, number density (number of that boundary type per square micron), length density (length of that boundary type per square micron), average length (total length divided by total number of that boundary type) and triple junction density (number of a certain triple junction type per square micron). Each parameter has the practical meaning, for example, the average length of carbide/binder phase boundaries would illustrate the wetting effect of binder phase to carbide crystals. Therefore, the outcome of these stereological statistics would quantitatively illustrate the components as well as spatial distribution features of boundaries, and in turn would provide significant clues for surveying the structure-property relationship of cemented carbides.

VII. Summaries

This work reviews the interdisciplinary approach of simultaneous use of the statistical FPA method and the GBCD in cemented carbides.

(1) There exist crystals as well as boundary networks and consequently there exist orientation texture of crystals as well as orientation texture of boundary planes. 50 kinds of CSL boundaries can occur theoretically in cemented carbides, and $\Sigma 2$ boundary that has a $90°/[10\bar{1}0]$

misorientation is the most frequently occurring boundary type in cemented carbides.

(2) In the FPA method, three Eulerian angles (marked as Δg) are used to describe the misorientation across the boundary plane, and two angular parameters (marked as n) are used to describe the direction of boundary plane normal in the crystallographic frame.

(3) The $\lambda(\Delta g, n)$ mode of the FPA method takes both Δg and n into account and the corresponding result illustrates the orientation texture for boundary planes with the specific misorientation. The peak position, the MRD value and the spreads between the peak positions should be evaluated in a $\lambda(\Delta g, n)$ pole plot.

(4) The $\lambda(n)$ mode of the FPA method ignores Δg and merely takes n into account and accordingly, the result illustrates the orientation texture of habit planes and in turn, the shape anisotropy of carbide crystals.

(5) Both the $\lambda(\Delta g, n)$ mode and the $\lambda(n)$ mode of the FPA method can be used in a series of samples, and the results can illustrate the change of GBCD along with the variation of processing/application factors.

(6) The whole boundaries can be divided into different subsets according to the specific misorientation relationship, misorientation angle range, or the phase attribute on the two sides of the boundary plane. Along with new stereological statistics from planar EBSD data, boundary sort methods before use of the FPA method facilitate the investigation of boundaries with specific attributes. In all, the interdisciplinarity between the FPA method and the GBCD develops the knowledge about the structure-property relationship in cemented carbide.

References

1. D.H. Warrington, "The coincidence site lattice (CSL) and grain boundary (DSC) dislocations for the hexagonal lattice", *J. Phys. Colloques.*, **36** [c4] (1975) 87–95.
2. J. Vicens, S. Lay, M. Benjdir, G. Nouet, "Nature of the boundary planes in tungsten carbide-cobalt composites", *J. Phys. Colloques.*, **51** [c1] (1990) 353–358.
3. S. Hagege, G. Nouet, P. Delavignette, "Grain boundary analysis in TEM. IV. Coincidence and the associated defect structure in tungsten carbide", *Phys. Stat. Sol. A*, **62** [1] (2010) 97–107.
4. J.K. Mackenzie, M.J. Thomson, "Some statistics associated with the random disorientation of cubes", *Biometrika*, **44** [1-2] (1957) 205–210.
5. J. Vicens, E.L. Pinson, J.L. Chermant, G. Nouet, "Structural analysis and properties of grain boundaries in hexagonal carbides", *J. Phys. Colloques.*, **49** [C5] (1988) 271–276.
6. J. Vicens, M. Benjdir, G. Nouet, A. Dubon, J.Y. Laval, "Cobalt intergranular segregation in WC-Co composites", *J. Mater. Sci.*, **29** [4] (1994) 987–994.
7. T. Yamamoto, Y. Ikuhara, T. Watanabe, T. Sakuma, Y. Taniuchi, "High resolution microscopy study in Cr_3C_2-doped WC-Co", *J. Mater. Sci.*, **36** [16] (2001) 3885–3890.
8. M.U. Farooq, U. Klement, "EBSD characterization of carbide-carbide boundaries in WC-Co composites", *J. Microsc.*, **213** [3] (2004) 306–312.
9. R.C. Pond, A. Serra, D.J. Bacon, "Dislocations in interfaces in the *h.c.p.* metals-II. Mechanisms of defect mobility under stress", *Acta. Mater.*, **47** [5] (1999) 1441–1453.
10. J. Kishino, H. Nomura, S.G. Shin, H. Matsubara, T. Tanase, "Computational study on grain growth in cemented carbides", *Int. J. Refract. Met. Hard Mater.*, **20** [1] (2002) 31–40.
11. J.D. Kim, S.J.L. Kang, J.W. Lee, "Formation of grain boundaries in liquid phase sintered WC-Co alloys", *J. Am. Ceram. Soc.*, **88** [2] (2010) 500–503.
12. G. Ostberg, M.U. Farooq, Mikael Christensen, H.O. Andren, U. Klement, G. Wahnstrom. "Effect of Σ2 grain boundaries on plastic deformation of WC-Co cemented carbides", *Mater. Sci. Eng. A*, **416** [1-2] (2006) 119–125.
13. M. Christensen, S. Dudiy, G. Wahnstrom, "First-principles simulations of metal-ceramic interface adhesion: Co/WC versus Co/TiC", *Phys. Rev. B*, **65** (2002) 045408.
14. M. Christensen, G. Wahnstrom, "Effects of cobalt intergranular segregation on interface energetics in WC-Co", *Acta. Mater.*, **52** [8] (2011) 2199–2207.
15. M. Christensen, G. Wahnstrom, "Co-phase penetration of $WC(10\bar{1}0)/WC(10\bar{1}0)$ grain boundaries from first principles", *Phys. Rev. B*, **67** (2003) 115415.
16. M.A. Gren, G. Wahnstrom, "Wetting of surfaces and grain boundaries in cemented carbides and the effect from local chemistry", *Materialia*, **8** [1] (2019) 100470.
17. S.A.E. Johansson, G. Wahnstrom, "First-principles study of an interfacial phase diagram in the V-doped WC-Co system", *Phys. Rev. B*, **86** (2012) 035403.
18. S.A.E. Johansson, G. Wahnstrom, "First-principles derived complexion diagrams for phase boundaries in doped cemented carbides", *Curr. Opin. Solid State Mater. Sci.*, **20** [5] (2016) 299-307.
19. X.W. Liu, X.M. Liu, H. Lu, H.B. Wang, C. Hou, X.Y. Song, Z.R. Nie, "Low-energy grain boundaries in WC-Co cemented carbides", *Acta Mater.*, **175** (2018) 171–181.
20. X.W. Liu, X.Y. Song, HB, X.M. Liu, F.W. Tang, H. Lu, "Complexions in WC-Co cemented carbides", *Acta. Mater.*, **149** (2018) 164–178.
21. S. Lay, M. Loubradou, S.A.E. Johansson, G. Wahnstrom, "Interface structure in a WC-Co alloy co-doped with VC and Cr_3C_2", *J. Mater. Sci.*, **47** (2012) 1588–1593.
22. X.K. Yuan, J. Zhu, "Anisotropic distribution of phase boundaries and its potential correlation with magnetic properties in a sintered NdFeB permanent magnet", *Phys. Stat. Sol. B*, **257** (2020) 1900326.
23. M. Christensen, G. Wahnstrom, "Strength and reinforcement of interfaces in cemented carbides", *Int. J. Refract. Met. Hard Mater.*, **24** [1-2] (2006) 80–88.
24. E. Fransson, M.A. Gren, H. Larsson, G. Wahnstrom, "First-principles modeling of complexions at the phase boundaries in Ti-doped WC-Co cemented carbides at finite temperatures", *Phys. Rev, Mater.*, **5** (2021) 093801.
25. M. Christensen, G. Wahnstrom, C.H. Allibert, S. Lay, "Quantitative analysis of WC grain shape in sintered WC-co cemented carbides", *Phys. Rev. Lett.*, **94** [6] (2005) 066105.

26. M. Christensen, G. Wahnstrom, S. Lay, G.H. Allibert, "Morphology of WC grains in WC-Co alloys: Theoretical determination of grain shape", *Acta. Mater.*, **55** [5] (2007) 1515–1521.

27. S. Lay, C.H. Allibert, M. Christensen, G. Wahnstrom, "Morphology of WC grains in WC-Co alloys", *Mater. Sci. Eng. A*, **486** [1-2] (2008) 253–261.

28. T. Watanabe, "The impact of grain boundary character distribution on fracture in polycrystals", *Mater. Sci. Eng. A*, **176** [1-2] (1994) 39–49.

29. T. Watanabe, "Grain boundary engineering: historical perspective and future prospects", *J. Mater. Sci.*, **46** [12] (2011) 4095–4115.

30. V. Kumar, Z.G.F. Zak, S.I. Wright, M.M. Nowell, "An analysis of grain boundaries and grain growth in cemented tungsten carbide using orientation imaging microscopy", *Mettal. Mater. Trans. A*, **37** [3] (2006) 599–607.

31. V. Kumar, Z.G.F. Zak, S.I. Wright, M.M. Nowell, "A grain boundary analysis of cemented tungsten carbides using OIM", pp. 291–304 in *Applications of Texture Analysis*, Chapter 31. Ed. A.D. Rollett, John Wiley & Sons, Weinheim, Germany, 2008.

32. K. Mannesson, M. Elfwing, A. Kusoffsky, S. Norgren, J. Agren, "Analysis of WC grain growth during sintering using electron backscatter diffraction and image analysis", *Int. J. Refract. Met. Hard Mater.*, **26** [5] (2008) 449–455.

33. K.P. Mingard, B. Roebuck, E.G. Bennett, M.G. Gee, H. Nordenstrom, G. Sweetman, P. Chan, "Comparison of EBSD and conventional methods of grain size measurement of hardmetals", *Int. J. Refract. Met. Hard Mater.*, **27** (2009) 213–223.

34. K.P. Mingard, B. Roebuck, E.G. Bennett, M. Thomas, B.P. Wynne, E.J. Thomas, "Grain size measurement by EBSD in complex hot deformed metal alloy microstructures", *J. Microsc.*, **227** [3] (2010) 298–308.

35. B. Roebuck, K.P. Mingard, H.G. Jones, E.G. Bennett, "Aspects of the metrology of contiguity measurements in WC based hard materials", *Int. J. Refract. Met. Hard Mater.*, **62** (2017) 161–169.

36. X.W. Liu, X.Y. Song, H.B. Wang, C. Hou, X.M. Liu, X.L. Wang, "Reinforcement of tungsten carbide grains by nanoprecipitates in cemented carbides", *Nanotechnology*, **27** [41] (2016) 415710.

37. B. Roebuck, P. Klose, K.P. Mingard, "Hardness of hexagonal tungsten carbide crystals as a function of orientation", *Acta. Mater.*, **60** [17] (2012) 6131–6143.

38. M.G. Gee, K.P. Mingard, B. Roebuck, "Application of EBSD to the evaluation of plastic deformation in the mechanical testing of WC/Co hardmetal", *Int. J. Refract. Met. Hard Mater.*, **27** [2] (2009) 300–312.

39. K.P. Mingard, M.G. Gee, "EBSD examination of worn WC/Co hardmetal surfaces", *Wear*, **263** [1] (2007) 643–652.

40. I. Borgh, P. Hedstrom, J. Odqvist, A. Borgenstam, J. Agren, A. Gholinia, B. Winiarski, P.J. Withers, G.E. Thompson, K.P. Mingard, M.G. Gee, "On the three-dimensional structure of WC grains in cemented carbides", *Acta. Mater.*, **61** [13] (2013) 4726–4733.

41. K.P. Mingard, H.G. Jones, M.G. Gee, "Metrological challenges for reconstruction of 3-D microstructures by focused ion beam tomography methods", *J. Microsc.*, **253** [2] (2014) 93–108.

42. B. Winiarski, A. Gholinia, K.P. Mingard, M.G. Gee, G.E. Thompson, P.J. Withers, "Broad ion beam serial section tomography", *Ultramicroscopy*, **172** (2017) 52–64.

43. K.P. Mingard, H.G. Jones, M.G. Gee, B. Roebuck, J.W. Nunn, "*In-situ* observation of crack growth in a WC-Co hardmetal and characterisation of crack growth morphologies by EBSD", *Int. J. Refract. Met. Hard Mater.*, **36** (2013) 136–142.

44. M.G. Gee, K.P. Mingard, J.W. Nunn, B. Roebuck, A. Gant, "*In situ* scratch testing and abrasion simulation of WC/Co", *Int. J. Refract. Met. Hard Mater.*, **62** (2017) 192–201.

45. A. Meingast, E. Coronel, A. Blomqvist, S. Norgren, G. Wahnstrom, M. Lattemann, "High resolution STEM investigation of interface layers in cemented carbides", *Int. J. Refract. Met. Hard Mater.*, **72** (2017) 135–140.

46. S.A.E. Johansson, G. Wahnstrom, "A computational study of thin cubic carbide films in WC/Co interfaces", *Acta. Mater.*, **59** [1] (2011) 171–181.

47. S.A.E. Johansson, M.V.G. Petisme, G. Wahnstrom, "A computational study of special grain boundaries in WC-Co cemented carbides", *Comp. Mater. Sci.*, **98** (2015) 345–353.

48. M.V.G. Petisme, S.A.E. Johansson, G. Wahnstrom, "A computational study of interfaces in WC-Co cemented carbides", *Model. Simul. Mater. Sci.*, **23** [4] (2015) 045001.

49. M.A. Gren, E. Fransson, G. Wahnstrom, "A computational study of the temperature dependence of interface and surface energies in WC-Co cemented carbides", *Int. J. Refract. Met. Hard Mater.*, **87** (2020) 105114.

50. M.V.G. Petisme, M.A. Gren, G. Wahnstrom, "Molecular dynamics simulation of WC/WC grain boundary sliding resistance in WC-Co cemented carbides at high temperature", *Int. J. Refract. Met. Hard Mater.*, **49** (2015) 75–80.

51. U.A. Ozden, K.P. Mingard, M. Zivcec, A. Bezold, C. Broeckmann, "Mesoscopical finite element simulation of fatigue crack propagation in WC/Co-hardmetal", *Int. J. Refract. Met. Hard Mater.*, **49** [1] (2015) 261–267.

52. M. Ohman, M. Ekh, F. Larsson, G. Wahnstrom, "Finite element simulations of thermal residual stresses in realistic 3D WC-Co microstructures", *Int. J. Refract. Met. Hard Mater.*, **85** (2019) 105065.

53. S.A.E. Johansson, M. Ohman, M. Ekh, G. Wahnstrom, "CCBuilder: a software that produces synthetic microstructures of WC-Co cemented carbides", *Int. J. Refract. Met. Hard Mater.*, **78** (2019) 210–218.

54. D. Wolf, J.F. Lutsko, "On the geometrical relationship between tilt and twist grain boundaries", *Z. Kristallogr.*, **189** [3-4] (1989) 239–262.

55. D.M. Saylor, B.S.E. Dasher, B.L. Adams, G.S. Rohrer, "Measuring the five-parameter grain-boundary distribution from observations of planar sections", *Metall. Mater. Trans. A*, **35** [7] (2004) 1981–1989.

56. G.S. Rohrer, V. Randle, "Measurement of the five-parameter grain boundary distribution from planar sections", pp. 215–229 in *Electron Backscatter Diffraction in Materials Science*, Chapter 16, 2nd Edition. Eds. A.J. Schwartz, M. Kumar, B.L. Adams, D.P. Field Boston, MA: Springer, 2009.

57. K. Glowinski, A. Morawiec, "A toolbox for geometric grain boundary characterization", pp. 1–10 in *Proceedings of the 1st International Conference on 3D Materials Science*, Chapter 18. Eds. M.D. Graef, H.F. Poulsen, A. Lewis, J. Simmons, G. Spanos, USA-PA, Springer Inter-

national Publishing, 2012.

58. K. Glowinski, A. Morawiec, "Twist, tilt, and symmetric grain boundaries in hexagonal materials", *J. Mater. Sci.*, **49** (2014) 3936–3942.

59. C.S. Kim, G.S. Rohrer, "Geometric and crystallographic characterization of WC surfaces and grain boundaries in WC-Co composites", *Interface Sci.*, **12** (2004) 19–27.

60. C.S. Kim, T.R. Massa, G.S. Rohrer, "Modeling the influence of orientation texture on the strength of WC-Co composites", *J. Am. Ceram. Soc.*, **90** [1] (2007) 199–204.

61. C.S. Kim, T.R. Massa, G.S. Rohrer, "Interface character distributions in WC-Co composites", *J. Am. Ceram. Soc.*, **91** [3] (2010) 996–1001.

62. J.A. Klostermann, "The concept of the habit plane and the phenomenological theories of the martensite transformation", *J. Less-Common Met.*, **28** [1] (1972) 75–94.

63. D.M. Saylor, G.S. Rohrer, "Determining crystal habits from observations of planar sections", *J. Am. Ceram. Soc.*, **85** [11] (2002) 2799–2804.

64. X.K. Yuan, G.S. Rohrer, X.Y. Song, H. Chien, J. Li, "Modeling the interface area aspect ratio of carbide grains in WC-Co composites", *Int. J. Refract. Met. Hard Mater.*, **44** (2014) 7–11.

65. Y. Zhong, H. Zhu, L.L. Shaw, R. Ramprasad, "The equilibrium morphology of WC particles – A combined *ab* initio and experimental study", *Acta. Mater.*, **59** [9] (2011) 3748–3757.

66. L.L. Shaw, H. Luo, Y. Zhong, "WC-18 wt.% Co with simultaneous improvements in hardness and toughness derived from nanocrystalline powder", *Mater. Sci. Eng. A*, **537** (2012) 39–48.

67. X.K. Yuan, Y. Ji, "Characterization and analysis of aspect ratio of carbide grains in WC-Co composites", *RSC Adv.*, **8** [60] (2018) 34468–34475.

68. S.X. Zhao, X.Y. Song, C.B. Wei, L. Zhang, X.M. Liu, J.X. Zhang, "Effects of WC particle size on densification and properties of spark plasma sintered WC-Co cermet", *Int. J. Refract. Met. Hard Mater.*, **27** [6] (2009) 1014–1018.

69. X.K. Yuan, "Grain boundary character distributions of coincidence site lattice boundaries in WC-Co composites with different WC grain sizes", *J. Alloy Compd.*, **579** (2013) 622–627.

70. K.P. Mingard, B. Roebuck, J. Marshall, G. Sweetman, "Some aspects of the structure of cobalt and nickel binder

phases in hardmetals", *Acta. Mater.*, **59** [6] (2011) 2277–2290.

71. X.K. Yuan, C.B. Wei, D.T. Zhang, J. Zhu, X.X. Gao, "Characterization and comparison of grain boundary character distributions in cemented carbides with different binder phases", *Comp. Mater. Sci.*, **93** (2014) 144–150.

72. X.K. Yuan, "Effect of different binder phases on the Σ2 grain boundary plane distribution in tungsten carbides", *J. Superhard Mater.*, **41** [4] (2019) 229–236.

73. C.B. Wei, X.Y. Song, J. Fu, X.M. Liu, Y. Gao, H.B. Wang, S.X. Zhao, "Microstructure and properties of ultrafine cemented carbides-Differences in spark plasma sintering and sinter-HIP", *Mater. Sci. Eng. A*, **552** (2012) 427–433.

74. X.K. Yuan, X.Y. Song, H. Chien, J. Li, G.S. Rohrer, "Effect of densification mechanism on the Σ2 grain boundary plane distribution in WC-Co composites", *Mater. Lett.*, **92** (2013) 86–89.

75. X.K. Yuan, "Grain boundary character distributions of sigma2 boundaries in WC-Co composites with different cobalt volume fractions", *Ceram. Int.*, **40** [1] (2014) 1873–1878.

76. X.L. Wang, X.Y. Song, H.B. Wang, X.W. Liu, G.S. Guo, "Distribution of CSL grain boundaries in oriented cemented carbides", *CrystEngComm*, **18** [3] (2016) 471–479.

77. J.D. Bolton, M. Redington, "Plastic deformation mechanisms in tungsten carbide", *J. Mater. Sci.*, **15** [12] (1980) 3150–3156.

78. G. Ostberg, K. Buss, M. Christensen, S. Norgren, H.O. Andren, D. Mari, G. Wahnstrom, I. Reineck, "Mechanisms of plastic deformation of WC-Co and Ti(C, N)-WC-Co", *Int. J. Refract. Met. Hard Mater.*, **24** [1-2] (2006) 135–144.

79. G. Ostberg, K. Buss, M. Christensen, S. Norgren, H.O. Andren, D. Mari, G. Wahnstrom, I. Reineck, "Effect of TaC on plastic deformation of WC-Co and Ti(C,N)-WC-Co", *Int. J. Refract. Met. Hard Mater.*, **24** (2006) 145–154.

80. X.K. Yuan, G.S. Rohrer, X.Y. Song, H. Chien, J. Li, C.B. Wei, "Effect of plastic deformation on the Σ2 grain boundary plane distribution in WC-Co cemented carbides", *Int. J. Refract. Met. Hard Mater.*, **47** (2014) 38–43.

81. X.K. Yuan, X.H. Zhang, S.X. Deng, "Grain boundary character distributions of coincidence site lattice boundaries in WC-Co composites under plastic deformation", *Rare Metal Mat. Eng.*, **48** [8] (2019) 2454–2459.